4-20-2005

Numerical Solutions of the Three-Dimensional Magnetohydrodynamic **A** Model

Pablo D. Mininni
National Center for Atmospheric Re search

David C. Montgomery
Dartmouth College

Annick Pouquet
National Center for Atmospheric Re search

Numerical solutions of the three-dimensional magnetohydrodynamic alpha-model

Pablo D. Mininni[1], David C. Montgomery[2] and Annick Pouquet[1]
[1] *Advanced Study Program, National Center for Atmospheric Research, P.O. Box 3000, Boulder, Colorado 80307 and*
[2] *Dept. of Physics and Astronomy, Dartmouth College, Hanover, NH 03755*
(Dated: January 1, 2018)

We present direct numerical simulations and α-model simulations of four familiar three-dimensional magnetohydrodynamic (MHD) turbulence effects: selective decay, dynamic alignment, inverse cascade of magnetic helicity, and the helical dynamo effect. The MHD α-model is shown to capture the long-wavelength spectra in all these problems, allowing for a significant reduction of computer time and memory at the same kinetic and magnetic Reynolds numbers. In the helical dynamo, not only does the α-model correctly reproduce the growth rate of magnetic energy during the kinematic regime, but it also captures the nonlinear saturation level and the late generation of a large scale magnetic field by the helical turbulence.

PACS numbers: 47.27.Eq; 47.27.Gs; 47.11.+j

I. INTRODUCTION

The "alpha model," as it has come to be called in fluid mechanics, is a procedure whereby, by suppressing small spatial scales in a computation in a way that intends to do minimum damage to the accuracy with which the long wavelength spectral components are calculated, one can realize substantial savings in computing time [1, 2, 3, 4, 5, 6, 7, 8, 9, 10, 11, 12, 13]. In a previous paper [14], we gave a simple way to extend the alpha model to magnetohydrodynamics (see also [9, 10] for extensions in the non-dissipative case), we specialized it to two dimensions, and numerically tested its predictions in a series of computations. These were chosen as situations where direct numerical simulations (DNS) that started from identical initial conditions were feasible. The intent of this present paper is to present comparisons of the same kind for three-dimensional (3D) magnetohydrodynamics (MHD). This is a straightforward program in the light of the two-dimensional (2D) investigations [14] and we will draw heavily on the material in that paper to avoid repetition, but in 3D, new phenomena arise, such as the generation of magnetic fields through stretching by velocity gradients, and furthermore 3D is computationally more demanding than 2D.

In Section II, we take the 3D alpha model MHD equations [14] and describe briefly four problems upon which they will be tested against DNS treatments of the same problems. They are selective decay, dynamic alignment, the inverse cascade of magnetic helicity, and the mechanically driven turbulent dynamo. The first two have already been tested in 2D [14] and the third has a 2D analogue in the inverse cascade of magnetic vector potential [14]. The fourth is also not an unfamiliar effect, and we have recently been involved in addressing it for the special case of low magnetic Prandtl number [15] and for non-helical flows.

Our conclusions reached in Secs. III-VI are consistent for the most part with those reached for 2D MHD: the alpha model does a good job of reproducing the spectral behavior of the long-wavelength Fourier amplitudes (wavenumber $k \lesssim \alpha^{-1}$, where α is the spatial scale over which the velocity field and magnetic field are filtered). Because of the relative lack of surprises in the selective decay and dynamic alignment Sections, we rely on relatively brief presentations, to then focus in the study of the inverse cascade of magnetic helicity and the dynamo effect. Finally, we summarize the results in Sec. VII.

II. RELEVANT EQUATIONS; PROBLEMS CONSIDERED

In familiar "Alfvénic" dimensionless units, the original MHD equations are

$$\frac{\partial \mathbf{v}}{\partial t} + \mathbf{v}\cdot\nabla\mathbf{v} = -\nabla\mathcal{P} + \mathbf{j}\times\mathbf{B} - \nu\nabla\times\boldsymbol{\omega}, \quad (1)$$

$$\frac{\partial \mathbf{B}}{\partial t} + \mathbf{v}\cdot\nabla\mathbf{B} = \mathbf{B}\cdot\nabla\mathbf{v} - \eta\nabla\times\mathbf{j}, \quad (2)$$

together with $\nabla\cdot\mathbf{v} = 0 = \nabla\cdot\mathbf{B}$.

The velocity field is $\mathbf{v}$, the magnetic field is $\mathbf{B} = \nabla\times\mathbf{A}$, where $\mathbf{A}$ is the vector potential. The electric current density is $\mathbf{j} = \nabla\times\mathbf{B}$ and the vorticity is $\boldsymbol{\omega} = \nabla\times\mathbf{v}$. The dimensionless pressure, normalized to the (uniform) mass density is $\mathcal{P}$, and is obtained by taking the divergence of Eq. (1), using the incompressibility condition $\nabla\cdot\mathbf{v} = 0$, and solving the resulting Poisson equation. Removing a curl from Eq. (2) gives

$$\frac{\partial \mathbf{A}}{\partial t} = \mathbf{v}\times\mathbf{B} - \eta\mathbf{j} - \nabla\Phi, \quad (3)$$

where Φ is the scalar potential, obtainable also from a Poisson equation by imposing the Coulomb gauge $\nabla\cdot\mathbf{A} = 0$. The kinematic viscosity is ν and the magnetic diffusivity is η. In these dimensionless units, ν^{-1} can be interpreted as a Reynolds number $R_e = UL/\nu$ where in laboratory (c.g.s) units, U is a mean flow speed and L is a length characteristic of it. Similarly, η^{-1} can be interpreted as a magnetic Reynolds number $R_m = UL/\eta$. The magnetic Prandtl number is $P_m = \nu/\eta = R_m/R_e$.

In the alpha model the fields $\mathbf{v}$ and $\mathbf{B}$ are smoothed but $\boldsymbol{\omega}$ and $\mathbf{j}$ are not [14, 16]. The prescription is

$$\mathbf{u}_s = \int \mathrm{d}^3x' \, \frac{\exp\left[-|\mathbf{x}-\mathbf{x}'|/\alpha\right]}{4\pi\alpha^2|\mathbf{x}-\mathbf{x}'|}\mathbf{v}(\mathbf{x}',t) \quad (4)$$

$$\mathbf{B}_s = \int \mathrm{d}^3x' \, \frac{\exp\left[-|\mathbf{x}-\mathbf{x}'|/\alpha\right]}{4\pi\alpha^2|\mathbf{x}-\mathbf{x}'|}\mathbf{B}(\mathbf{x}',t). \quad (5)$$

Here α is an arbitrary filtering length, generally chosen smaller than the length scales one wishes to resolve. If $\mathbf{v}$ and $\mathbf{B}$ are Fourier-decomposed

$$\mathbf{v}(x,t) = \int \mathrm{d}^3k\ \mathbf{v}_\mathbf{k}(t)e^{i\mathbf{k}\cdot\mathbf{x}} \quad (6)$$

$$\mathbf{B}(x,t) = \int \mathrm{d}^3k\ \mathbf{B}_\mathbf{k}(t)e^{i\mathbf{k}\cdot\mathbf{x}}, \quad (7)$$

the connection between the Fourier transforms of the smoothed fields $\mathbf{u}_s$ and $\mathbf{B}_s$ and $\mathbf{v}_\mathbf{k}(t)$, $\mathbf{B}_\mathbf{k}(t)$ are

$$\mathbf{u}_s(\mathbf{k},t) = \mathbf{v}_\mathbf{k}(t)/(1+k^2\alpha^2) \quad (8)$$

$$\mathbf{B}_s(\mathbf{k},t) = \mathbf{B}_\mathbf{k}(t)/(1+k^2\alpha^2), \quad (9)$$

or in configuration space

$$\mathbf{v} = \left(1-\alpha^2\nabla^2\right)\mathbf{u}_s \quad (10)$$

$$\mathbf{B} = \left(1-\alpha^2\nabla^2\right)\mathbf{B}_s. \quad (11)$$

Note that we choose to smooth both the velocity and the magnetic field at the same length-scale, a choice appropriate for the unit magnetic Prandtl number ($\nu=\eta$) cases treated in this paper (for a different choice, see [15]).

The dynamics of the alpha model [14] amount to solving the pair,

$$\frac{\partial\mathbf{v}}{\partial t}+\mathbf{u}_s\cdot\nabla\mathbf{v} = -v_j\nabla u_s^j-\nabla\widetilde{\mathcal{P}}+\mathbf{j}\times\mathbf{B}_s -\nu\nabla\times\boldsymbol{\omega}, \quad (12)$$

$$\frac{\partial\mathbf{B}_s}{\partial t}+\mathbf{u}_s\cdot\nabla\mathbf{B}_s = \mathbf{B}_s\cdot\nabla\mathbf{u}_s-\eta\nabla\times\mathbf{j}, \quad (13)$$

where it is to be emphasized that in Eqs. (12,13), $\mathbf{v}$, $\mathbf{j}$, and $\boldsymbol{\omega}$ are not smoothed. $\widetilde{\mathcal{P}}$ is to be determined, as before, from the relevant Poisson equation.

In rectangular periodic boundary conditions (which we employ throughout), the ideal ($\nu=0=\eta$) invariants that have been identified for Eqs. (12,13) are the energy E

$$E=\frac{1}{2}\int\left(\mathbf{u}_s\cdot\mathbf{v}+\mathbf{B}\cdot\mathbf{B}_s\right)\mathrm{d}^3x, \quad (14)$$

the cross helicity H_C,

$$H_C=\frac{1}{2}\int\mathbf{v}\cdot\mathbf{B}_s\,\mathrm{d}^3x, \quad (15)$$

and the magnetic helicity H_M,

$$H_M=\frac{1}{2}\int\mathbf{A}_s\cdot\mathbf{B}_s\,\mathrm{d}^3x. \quad (16)$$

In the presence of non-zero η and ν, the decay rates for E, H_C, and H_M can readily been shown to be

$$\frac{\mathrm{d}E}{\mathrm{d}t} = -\nu\int\boldsymbol{\omega}_s\cdot\boldsymbol{\omega}\,\mathrm{d}^3x-\eta\int j^2\,\mathrm{d}^3x \quad (17)$$

$$\frac{\mathrm{d}H_C}{\mathrm{d}t} = -\frac{1}{2}\nu\int\boldsymbol{\omega}\cdot\mathbf{j}_s\,\mathrm{d}^3x-\frac{1}{2}\eta\int\boldsymbol{\omega}\cdot\mathbf{j}\,\mathrm{d}^3x \quad (18)$$

$$\frac{\mathrm{d}H_M}{\mathrm{d}t} = -\eta\int\mathbf{j}\cdot\mathbf{B}_s\,\mathrm{d}^3x \quad (19)$$

When we write $\boldsymbol{\omega}_s$ or $\mathbf{A}_s$, we mean that the same smoothing recipe as in Eqs. (4,5) has been applied to the unsmoothed fields $\boldsymbol{\omega}$ or $\mathbf{A}$. It is possible, and sometimes desirable, to use different smoothing lengths α_v, α_B for the mechanical and magnetic quantities [14, 15].

E, H_C and H_M as defined here are the ideal invariants of Eqs. (12,13), and reduce, as $\alpha\to 0$, to the usual ideal 3D MHD invariants. Sometimes, to make the global quantities agree at $t=0$ for initial-value runs, we may initially normalize the Fourier coefficients of the fields, by multiplication by a common factor, to bring E and H_C into exact initial agreement with the corresponding numbers for the ideal 3D MHD invariants (note that H_M involves two smoothed fields, and therefore can not be matched to the DNS initial conditions at the same time). Hereafter, such global quantities as E, H_C, etc., will be referred to unit volume.

It is well known that for decaying turbulent situations, the presence of enough initial H_M or H_C can lead to a late-time state in which the ratios $|H_M/E|$ or $|H_C/E|$ can be close to maximal. The first situation, called "selective decay," [17, 18, 19] leads to a late-time quasi-steady state in which the remaining energy is nearly all magnetic and is nearly all condensed into the longest wavelength modes allowed by the boundary conditions. The second situation, called "dynamic alignment," [20, 21, 22] leads to a late-time quasi-steady state in which $\mathbf{v}$ and $\mathbf{B}$ are nearly parallel or anti-parallel. In both cases, the states can be very long-lived because the nonlinear transfer to small scales has essentially been shut down ("suppression of nonlinearity"). We illustrate these two situations in Secs. III and IV.

Inverse cascade processes [23, 24, 25, 26] are those wherein excitations externally injected at the small scales are preferentially transferred to the larger scales and pile up there, creating coherent macroscopic structures at large scales where none were present initially. A quantity which can be inversely cascaded in 3D MHD is H_M [24, 25]. We illustrate this with an externally-driven run in Sec. V.

Dynamo processes (see Ref. [27] for a review) are those whereby mechanical injection of excitations transfer energy to magnetic fields, causing them to amplify. A novel example of helical dynamo action using the alpha-model is treated in Sec. VI.

In all four cases, well-resolved DNS solutions are regarded as baseline truths against which alpha-model computations are to be tested.

III. SELECTIVE DECAY

In selective decays, energy decays rapidly relative to magnetic helicity, if any [17, 18, 19]. In order to display the process most clearly, it helps to start an initial-value decay run with a significant amount of magnetic helicity. One way to accomplish this is to make the initial values of $\mathbf{v}$ and $\mathbf{B}$ out of

what are called "ABC" flows. We define

$$\begin{aligned}\mathbf{v}_{ABC} &= [B\cos(ky) + C\sin(kz)]\,\hat{x} + \\ &+ [A\sin(kx) + C\cos(kz)]\,\hat{y} + \\ &+ [A\cos(kx) + B\sin(ky)]\,\hat{z} \end{aligned} \quad (20)$$

for arbitrary real numbers A, B, C, and k. $\mathbf{v}_{ABC}$ is an eigenfunction of the curl. The specific initial conditions chosen are

$$\mathbf{v}(t=0) = \sum_{k=k_{bot}}^{k_{top}} v_0 \left[\mathbf{v}_{ABC}(k,\phi_k) + \hat{\mathbf{v}}(\mathbf{k})e^{i\mathbf{k}\cdot\mathbf{x}}\right] \quad (21)$$

$$\mathbf{B}(t=0) = \sum_{k=k_{bot}}^{k_{top}} b_0 \left[\mathbf{v}_{ABC}(k,\phi_k) + \hat{\mathbf{B}}(\mathbf{k})e^{i\mathbf{k}\cdot\mathbf{x}}\right]. \quad (22)$$

The notation $\mathbf{v}_{ABC}(k,\phi_k)$ means that for each $\mathbf{k}$ in the summation, a random phase ϕ_k is added to the arguments of the sines and cosines for that k. The summations are over all the $\mathbf{k}$ values (which lie on a lattice in $\mathbf{k}$ space defined by the periodic boundary conditions) between radii k_{bot} and k_{top}. The $\hat{\mathbf{v}}(\mathbf{k})$ and $\hat{\mathbf{B}}(\mathbf{k})$ represent added random perturbations.

Here, we have chosen $A = B = C = 1$, $k_{bot} = 6$, $k_{top} = 10$, and v_0, b_0 are chosen to make the initial $\langle v^2\rangle = \langle B^2\rangle = 1$, where "$\langle.\rangle$" means a spatial average over the basic box. It is also the case that initially, $\langle \mathbf{v}\cdot\mathbf{B}\rangle = 0$. Random modes $\hat{\mathbf{v}}(\mathbf{k})$ and $\hat{\mathbf{B}}(\mathbf{k})$ are added with an energetic level to initially give $\langle \mathbf{A}\cdot\mathbf{B}\rangle = 0.5\,\langle|\mathbf{A}||\mathbf{B}|\rangle$. The dimensionless inverse Reynolds numbers are $\nu = \eta = 0.002$.

Three runs for a typical case are displayed. The first of these is a well-resolved DNS run at a resolution of 256^3, with dealiasing achieved by zeroing out all Fourier coefficients with $k > 256/3$, a method that will be used throughout (usually referred to as the "$2/3$ rule"). Then two α-model runs are performed with the same initial conditions, a 128^3 run with $\alpha = 1/20$ and a 64^3 run with $\alpha = 1/10$. The same values of ν, η apply to all three runs. The caption of Fig. 1.a identifies the decaying energies (kinetic energy E_K and magnetic energy E_M) as functions of time. Fig. 1.b shows the ratio $\langle \mathbf{A}\cdot\mathbf{B}\rangle \,/\, \langle|\mathbf{A}||\mathbf{B}|\rangle$ as a function of time for the three runs; it has increased to above 0.999 by the final time.

Fig. 2 shows the (unnormalized) energies and magnetic helicities for the three runs. Note that by normalizing the DNS and α-model initial conditions to have equal energies, it has meant that the α-model magnetic helicities have necessarily started at lower initial values than those of the DNS.

Figs. 3 and 4 show the associated energy spectra plotted vs. wave number. Fig. 3 is at an early time ($t = 10$) and shows the total energy spectrum compensated by Kolmogorov's $-5/3$ law. Fig. 4 shows kinetic (E_K) and magnetic (E_M) energy spectra at a very late time ($t = 733$). The two values of α^{-1} are shown as vertical lines. Below $k \sim \alpha^{-1}$, the DNS and α-model agree reasonably well.

As follows from Figs. 2 and 4, at late times the magnetic field is concentrated at large scales ($k = 1$) and has maximum relative helicity (note that $E \sim E_M \sim H_M$ after $t \sim 200$ in both the DNS and alpha-model simulations). Fig. 5 shows surfaces of constant H_M at $t = 800$ in the 3D domain, for the DNS and the 64^3 alpha-model simulation. The alpha-model is able to reproduce the large scale structures observed in the DNS, and only slight differences can be observed. As will be shown in Section IV this is not always the case when using periodic boundary conditions (similar results were obtained in 2D MHD simulations [14]).

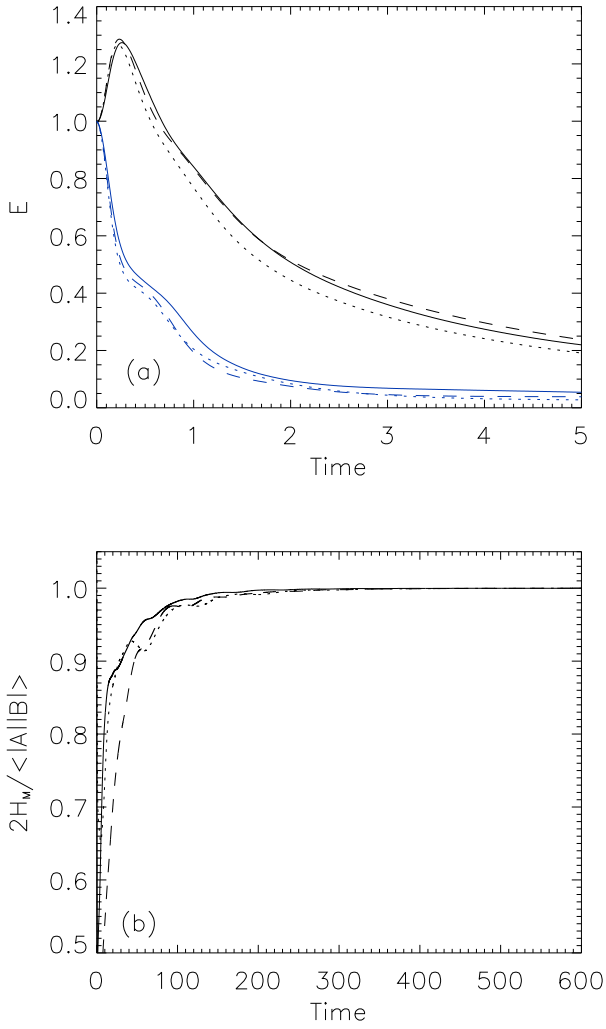

FIG. 1: (color online) (a) Magnetic energy (upper curves) and kinetic energy (lower blue curves) as a function of time until $t = 5$, and (b) relative magnetic helicity as a function of time until $t = 600$, for the selective decay runs. Solid lines correspond to DNS, dashed lines to 128^3 α-model simulations, and dotted lines to 64^3 α-model simulations.

IV. DYNAMIC ALIGNMENT

In this case, we load Fourier coefficients into the spherical shells with $k_{bot} = 6 \le k \le k_{top} = 10$ with equal amplitudes but enough correlation between the phases of $\mathbf{v}$ and $\mathbf{B}$ so that initially $\langle \mathbf{v}\cdot\mathbf{B}\rangle = 0.3\,\langle|\mathbf{v}||\mathbf{B}|\rangle$; otherwise the phases

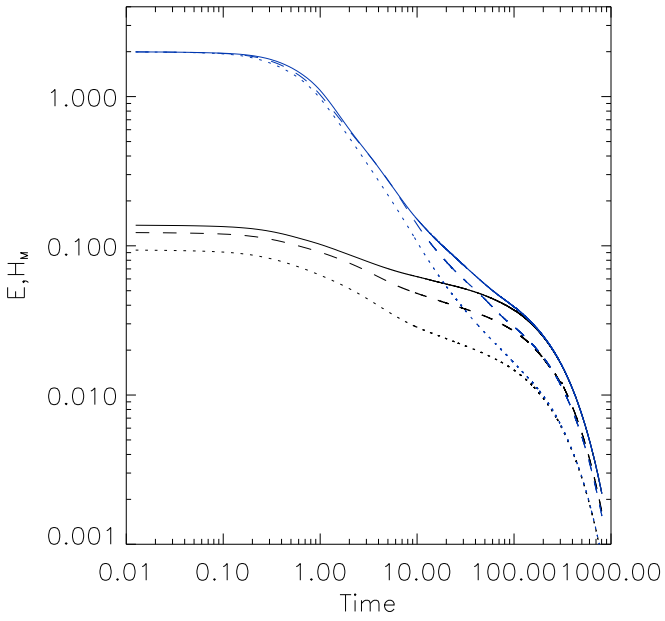

FIG. 2: (color online) Total energy (upper blue curves) and magnetic helicity (lower curves) as a function of time. Labels are as in Fig. 1.

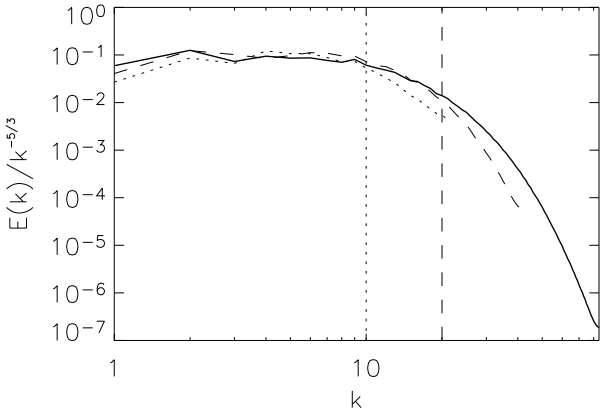

FIG. 3: Total energy spectrum compensated by Kolmogorov's $-5/3$ law, for the three dynamic alignment runs (labels are as in Fig. 1), at $t = 10$. Vertical dotted and dashed lines indicate respectively the scales $\alpha^{-1} = 10$ and 20.

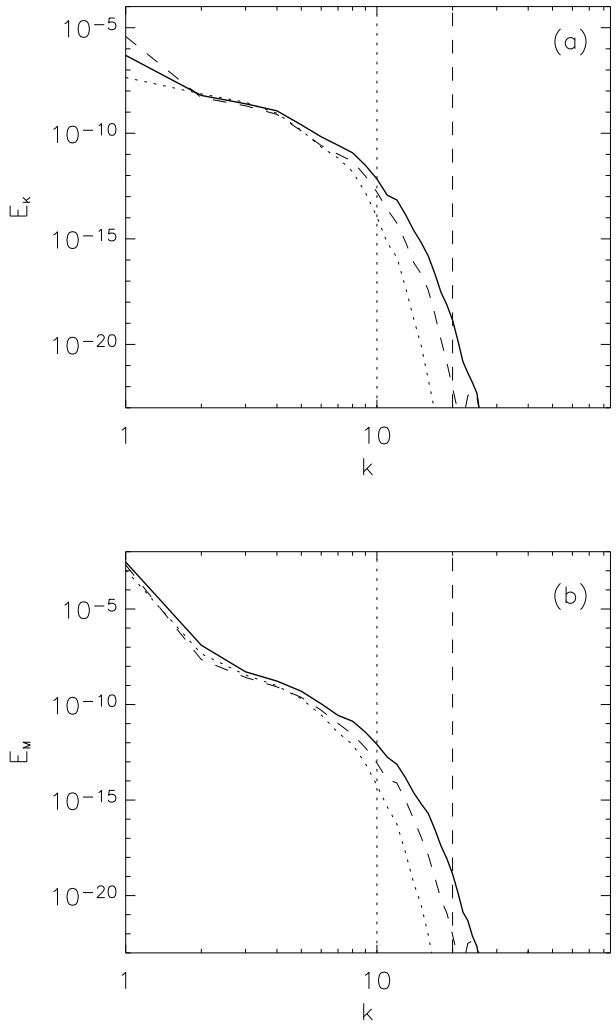

FIG. 4: (a) Kinetic and (b) magnetic energy spectra, for the three dynamic alignment runs (labels are as in Fig. 1), at $t = 733$.

are random. We again do a 256^3 DNS run, an α-model run at 128^3 with $\alpha = 1/20$, and another α-model run at 64^3 with $\alpha = 1/10$. For all three runs, $\nu = \eta = 0.002$. The same conventions are adopted for the graphics as in Sec. III.

Figs. 6a,b show the decay of the kinetic and magnetic energies (a), chosen initially to be equal; and (b) the degree of alignment, as measured by the mean cosine of the alignment angle, $\langle \mathbf{u}_s \cdot \mathbf{B} \rangle \,/\, \langle |\mathbf{u}_s||\mathbf{B}| \rangle$ that develops as a function of time. Since much of the alignment is contributed by the small scales, the α-model underestimates the degree of alignment, and the disparity becomes greater as α^{-1} is decreased, though the accuracy remains within the 10 percent level. Fig. 7 shows the decay of both E and H_c, with the more rapid decay of the former. There is, in this case, no preferential migration of any global quantity to long wavelengths.

Figures 8 and 9 show the kinetic and magnetic energy spectra at an early time, $t = 4.5$, and at a late one, $t = 156$. The agreement of the α-model and DNS for $k \lesssim \alpha^{-1}$ is again seen to be excellent except for an unexplained over-estimate at the earlier time $t = 4.5$ for the kinetic energy spectrum.

Fig. 10 shows surfaces of constant H_C at $t = 150$ in the 3D domain, for the DNS and the 64^3 alpha-model simulation. While there are marked similarities in the kinds of structures present in the DNS and in the alpha runs, there are no one-to-one correspondences as to specific features, either as to location or orientation. As in the 2D case [14] we conclude that in this case the alpha-model does an excellent job reproducing the statistical properties of the large-scale spectra, but

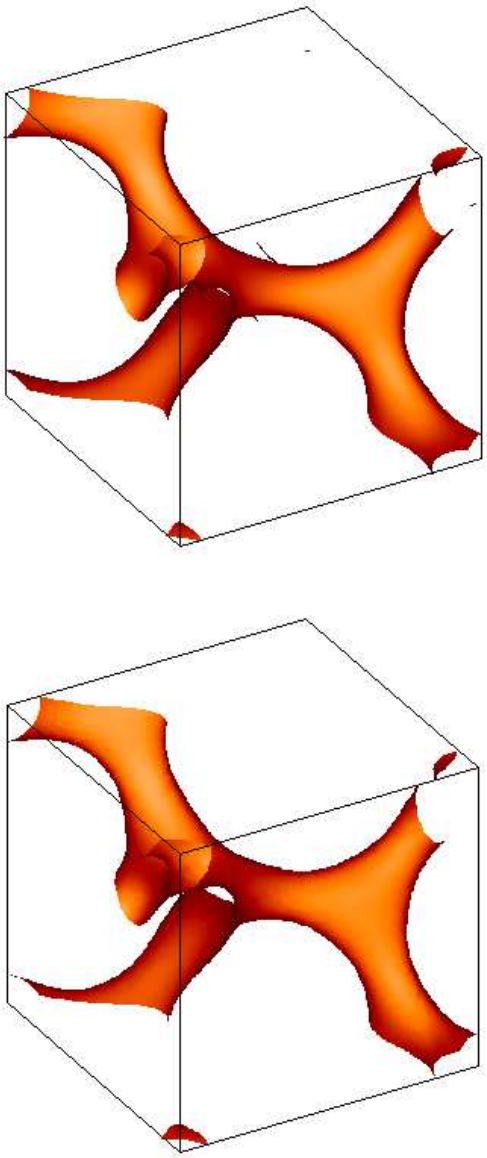

FIG. 5: (color online) Surfaces of constant magnetic helicity density at $t = 800$ at 90% of its maximum value, for the DNS (above), and the 64^3 alpha-model simulation (below).

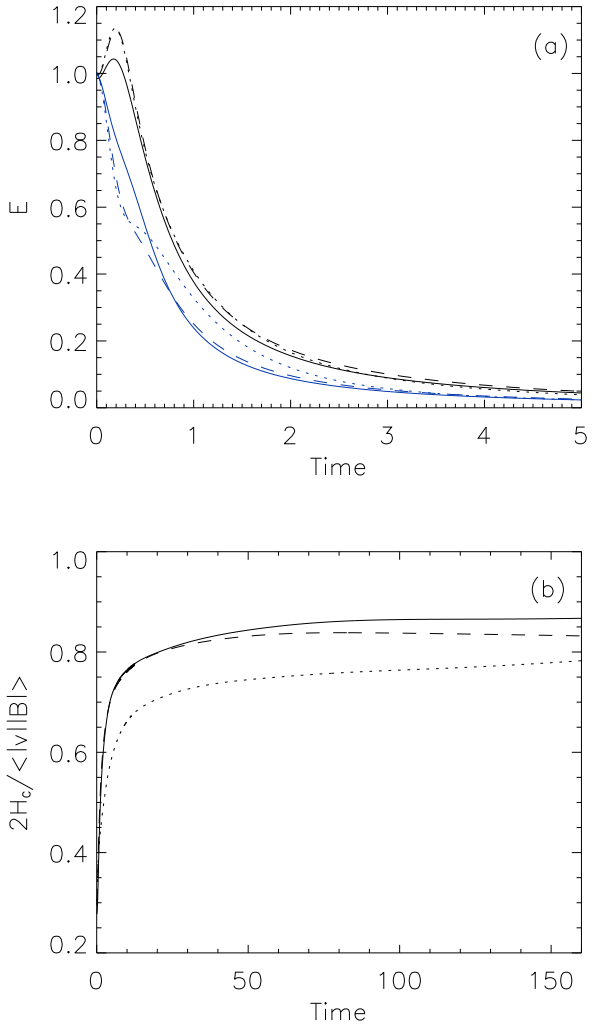

FIG. 6: (color online) (a) Magnetic energy (upper curves) and kinetic energy (lower blue curves) as a function of time until $t = 5$, and (b) relative cross helicity as a function of time until $t = 160$, for the dynamic alignment runs. Solid lines correspond to DNS, dashed lines to 128^3 α-model simulations, and dotted lines to 64^3 α-model simulations.

small-scale detailed phase information (such as the location of structures) is lost.

The reason for the striking agreement between the α-model and DNS exhibited in Fig. 5, as contrasted with the disagreement shown later in Fig. 10 is that in the case of selective decay, both computations have found the same final state: the isotropic, maximum-helicity, $k = 1$ state. This state is the "ABC flow" with A, B, and C all equal.

V. INVERSE CASCADES

Inverse cascades of magnetic helicity, driven mechanically at the small scales, have long been known to be an efficient dynamo mechanism for generating large-scale magnetic fields [28]. Here, we try a different approach: we drive the magnetic field directly at small scales with a random forcing function that is a superposition of "ABC" flows [see Eq. (20)] between wavenumbers $k = 8$ and 9, and with no driving for the velocity. The randomness is introduced by randomly changing the phases in the trigonometric arguments of each ABC component with a correlation time of $\Delta t = 1.25 \times 10^{-2}$ (in all the simulations we discuss in this section, the time step is 2.5×10^{-3}). A tiny seed velocity field is amplified some-

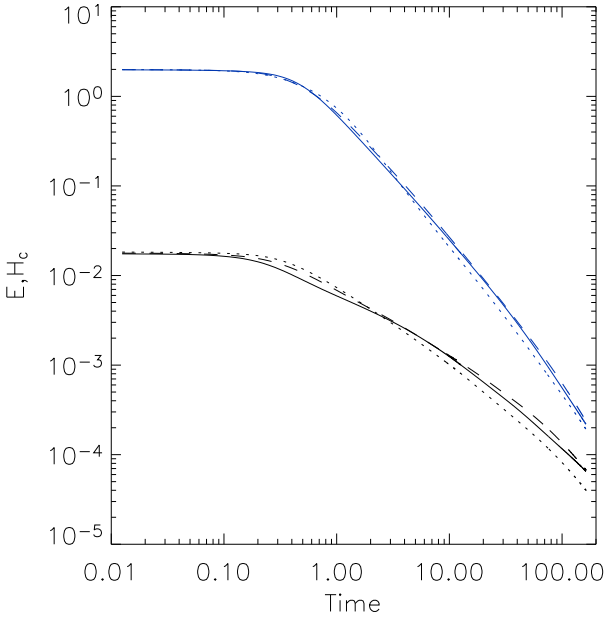

FIG. 7: (color online) Total energy (upper blue curves) and cross helicity (lower curves) as a function of time. Labels are as in Fig. 6.

what, but the kinetic energy always remains well below the level of the magnetic energy throughout. We again exhibit the results of a 256^3 DNS computation, and α-model computations with $\alpha = 1/20$ and $1/10$, with resolutions of 128^3 and 64^3 respectively.

Figs. 11 show the time histories of the energies (a) and magnetic helicities (b) for the three runs. The rather abrupt phase jumps in the ABC flows give the lines a jagged appearance and it is sometimes difficult to identify which of the three runs is which. Suffice it to say that the two α-model runs exhibit the same features as the DNS runs, but with a time lag that is greater for the larger α. This is visible more clearly in Fig. 12, where the magnetic helicity spectra for the three simulations are plotted as functions of k. The curves are the helicity spectra as functions of time. The lower levels of excitation are associated with earlier times. The times exhibited range from $t = 30$ to $t = 72.5$. The peak, once established, moves to the left with nearly the same speed in each case. The suppression of small scales, where the unsmoothed ABC flow is also unstable, may be responsible for the time lag. This time-lagged behavior is reminiscent of what happened in two dimensions with the inverse cascade of mean square vector potential [14]. However, note that in three dimensions once the inverse cascade has been established, the growth rate of magnetic helicity is well captured by the alpha-model (Fig. 11.b), indicative of a more local cascade (in scale). The power laws present in the spectra of magnetic helicity, and kinetic and magnetic energy [25] are also well captured by the alpha-model.

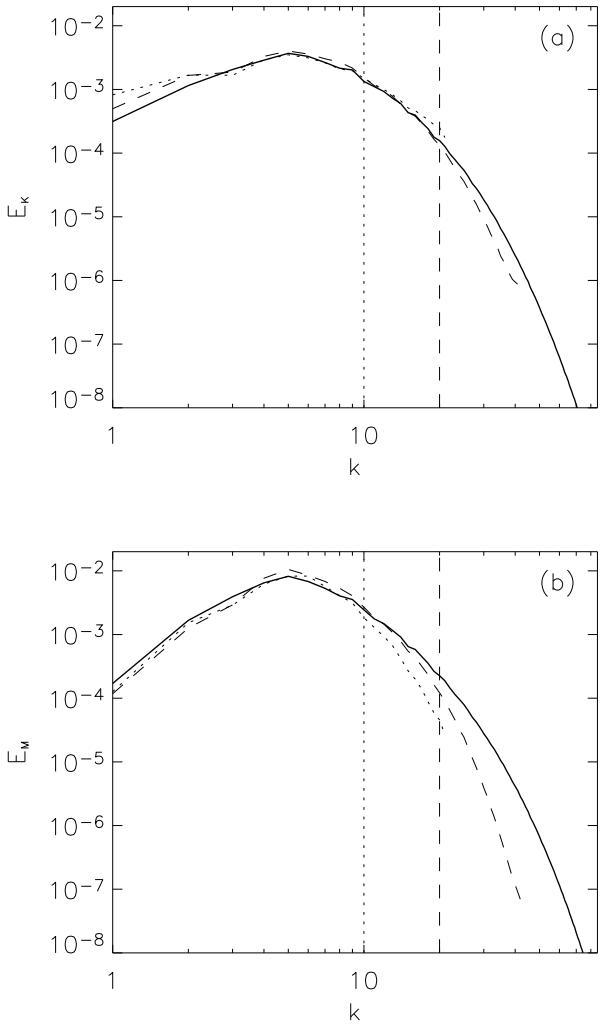

FIG. 8: (a) Kinetic and (b) magnetic energy spectra, for the three dynamic alignment runs (labels are as in Fig. 6), at $t = 4.5$. Vertical dotted and dashed lines indicate respectively the scales $\alpha^{-1} = 10$ and 20.

VI. THE DYNAMO

The mechanically-driven dynamo, in which injected mechanical energy is converted to magnetic energy at large scales, has long been a recurrent problem in MHD [27]. Here we are able to show that the alpha model yields the same results within acceptable accuracy as those of a DNS of the same situation (see Ref. [15] for another case of recent interest).

We begin with a velocity field which is again forced externally with the "ABC" geometry of Eq. (20). We choose $A = 0.9$, $B = 1.0$, and $C = 1.1$, $k_0 = 3$, with $\eta = \nu = 0.002$. This choice is governed by the knowledge that the $A = B = C$ flow gives the largest dynamo growth rate [29] but it is hydrodynamically very stable [30]; breaking that symmetry allows for turbulence to develop faster [31].

The force is allowed to operate until a statistically-steady

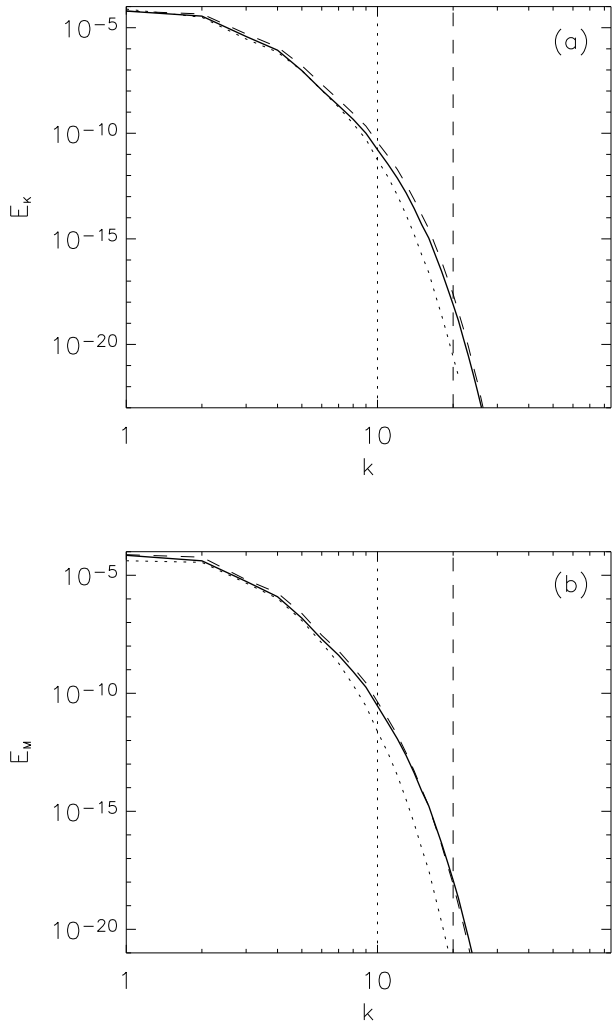

FIG. 9: (a) Kinetic and (b) magnetic energy spectra, for the three dynamic alignment runs.

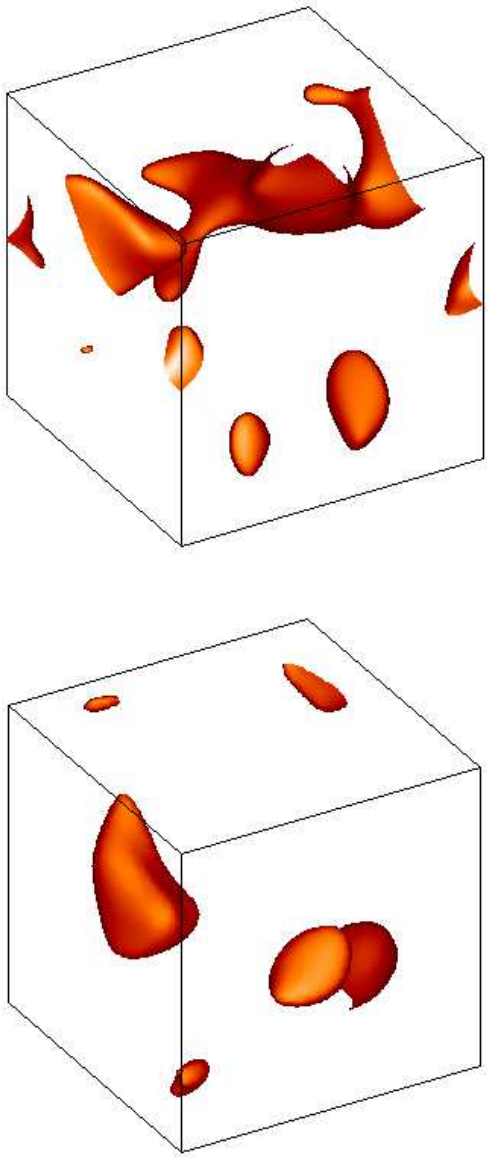

FIG. 10: (color online) Surfaces of constant cross helicity density at $t = 150$ at 50% of its maximum value, for the DNS (above), and the 64^3 alpha-model simulation (below).

turbulent Navier-Stokes flow prevails. Then a magnetic seed field is introduced at a very low level in the modes from $k = 1$ to $k = 10$. As in some other sections, we compare a DNS run at resolution 256^3 with two α-model runs, one with $\alpha = 1/20$ and 128^3 resolution, the other with $\alpha = 1/10$ and 64^3 resolution.

Before embarking on the MHD comparison between DNS and alpha-model results, it is instructive to compare the hydrodynamic properties of the flow. When the small magnetic seed is introduced, the Lorentz force in the Navier-Stokes equation can be neglected. The induction equation is linear in the magnetic field, and as a result, the geometrical properties of the flow are responsible for the observed amplification.

The flow generated by the external ABC force is helical. Previous studies of the alpha-model behavior in simulations of hydrodynamic flows were carried for non-helical flows [6, 13]. As a result, here we will focus only on the characterization of the flow helicity. The amount of helicity in a flow (both for DNS and the alpha-model [7]) is measured by the kinetic helicity

$$H_K = \frac{1}{2} \int \mathbf{v} \cdot \boldsymbol{\omega} \, \mathrm{d}^3 x \, . \tag{23}$$

It is also useful to normalize this quantity introducing the relative helicity $2H_K/(\langle|v|\rangle \langle|\omega|\rangle)$. Fig. 13 shows the probability distribution function (pdf) of relative kinetic helicity for the DNS and alpha-model simulations. A stronger positive tail can be identified in all cases, giving rise to a net positive kinetic helicity in the flow.

In 3D hydrodynamic turbulence, kinetic helicity is an ideal invariant and is known to cascade to smaller scales [32, 33].

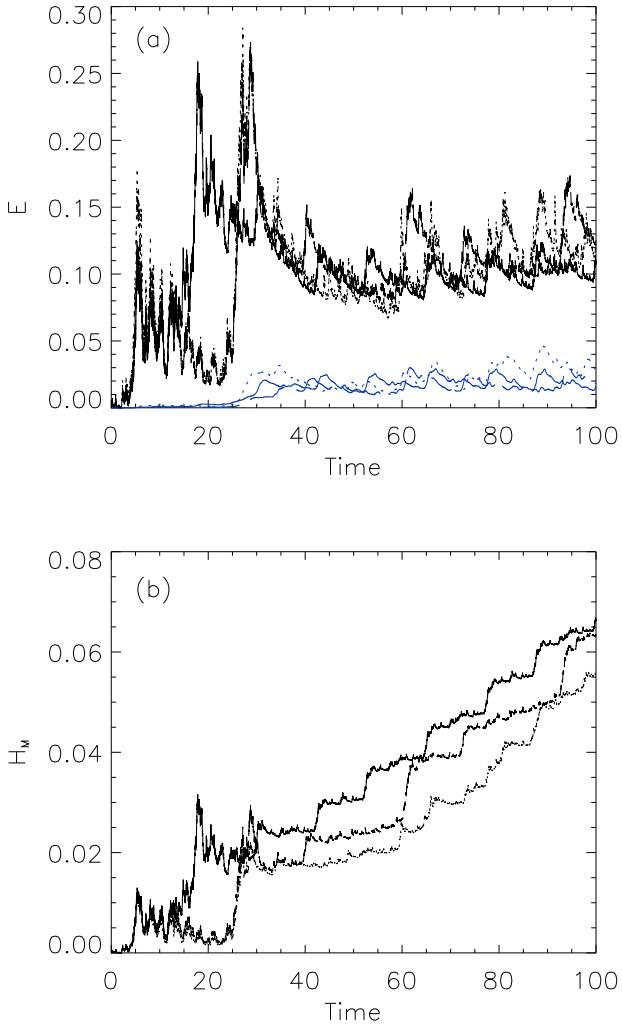

FIG. 11: (color online) (a) Magnetic energy (upper curves) and kinetic energy (lower blue curves) as a function of time, and (b) magnetic helicity as a function of time. Solid lines correspond to DNS, dashed lines to 128^3 α-model simulations, and dotted lines to 64^3 α-model simulations.

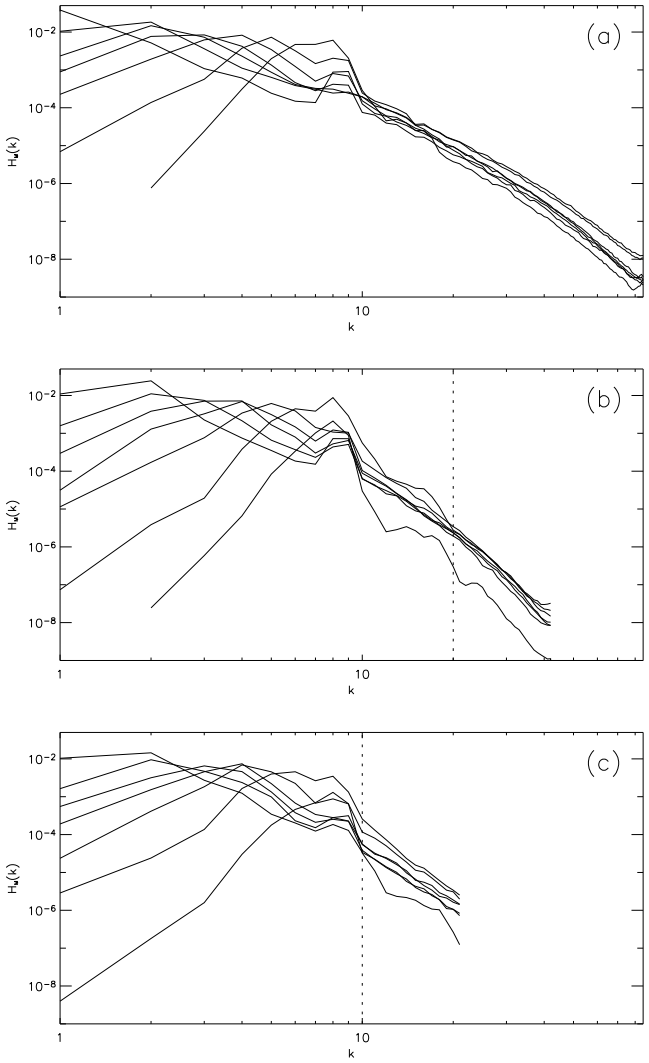

FIG. 12: Spectrum of magnetic helicity for different times, for $t =$ 30, 35, 40, 45, 55, and 72.5; (a) DNS, (b) 128^3 α-model, and (c) 64^3 α-model. The vertical lines indicate α^{-1}. Note the cascade of magnetic helicity to large scales as time evolves.

Fig. 14 shows the spectrum of H_K during the hydrodynamic simulation. As with the energy, the alpha-model is able to capture the evolution of kinetic helicity in Fourier space up to $k \sim \alpha^{-1}$. It seems that a Kolmogorov spectrum results for helicity [34, 35], which implies that the relative helicity is weaker at small scales.

The early stages of the growth of the magnetic field are in the "kinematic dynamo" parameter regime, involving exponential growth of the magnetic energy. This is shown in Fig. 15, which exhibits both the kinetic and magnetic energy as functions of time for the three runs. Though the three energies as functions of time are offset, it is clear that the linear growth rates are close. At about $t = 30$, there is a saturation, close to a state in which on the average the energy is equipartitioned approximately between kinetic and magnetic. After that, there are no significant variations in the evolution of the total kinetic and magnetic energy.

Figs. 16 and 17.a,b show the negative of the magnetic helicity, the mean square vector potential, and the mean square current density as functions of time. Though the agreements are not sharp, it is clear that the saturation levels and the times of saturation are both well approximated. Note that, in accord with expectations [36], the magnetic helicity acquires a negative value, opposite to the sign of the injected mechanical helicity. Note also that growth rates of both small scales (represented by the square current) and large scales (represented by the square vector potential) are well approximated by the alpha model during the kinematic regime.

While at $t \approx 30$ saturation in the exponential growth of magnetic energy takes place, the large scale modes continue growing, and at the end the magnetic field is dominated by

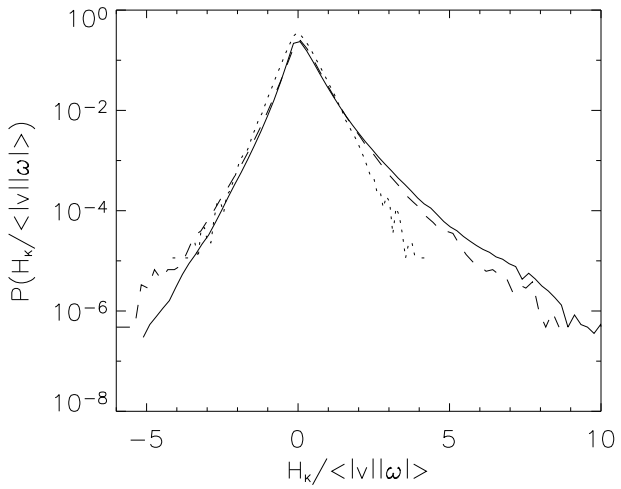

FIG. 13: Probability distribution function of relative kinetic helicity. Solid lines correspond to DNS, dashed lines to 128^3 α-model simulations, and dotted lines to 64^3 α-model simulations.

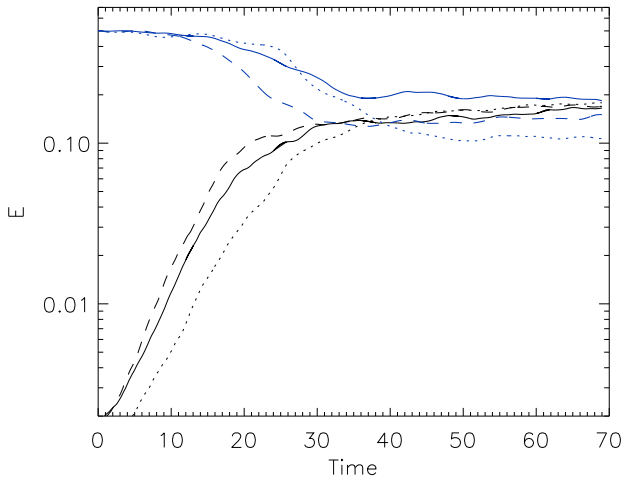

FIG. 15: (color online) Kinetic energy (upper blue curves) and magnetic energy (lower curves) as a function of time. Labels are as in Fig. 13.

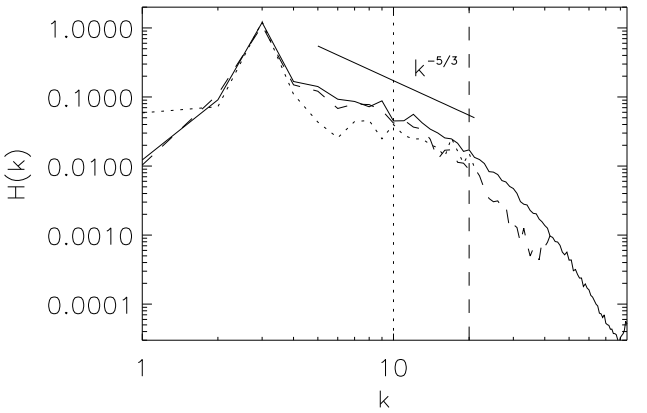

FIG. 14: Spectrum of kinetic helicity. The Kolmogorov's slope is shown as a reference. The vertical lines indicate α^{-1}. Labels are as in Fig. 13.

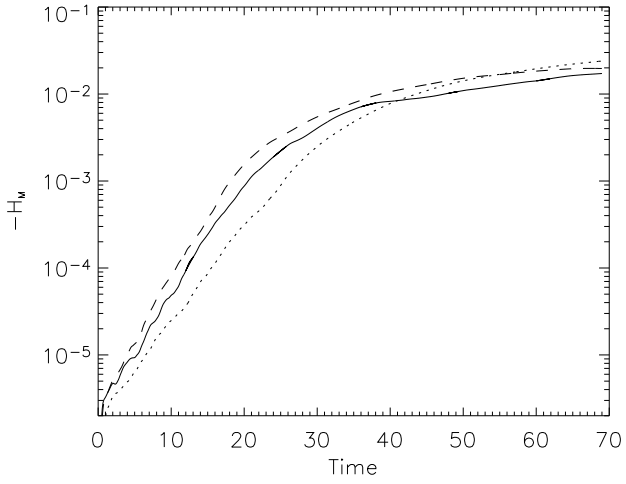

FIG. 16: Negative of the magnetic helicity as a function of time. Labels are as in Fig. 13.

large scales. While the mean square current density is constant after $t = 30$, the squared vector potential keeps growing slowly. This behavior is even clearer in the evolution of the magnetic energy spectrum.

Figs. 18.a,b show the evolution of the kinetic and magnetic spectra. The thick lines indicate kinetic spectra and the thin lines the magnetic spectra. The vertical lines indicate the locations of the two values of α^{-1}. In Fig. 18.a, the upper traces are the DNS spectrum at the time the seed field begins to grow, both for DNS and α-model simulations. The lower traces in Fig. 18.a show the magnetic spectrum at an early stage of its evolution. During this stage, the magnetic energy spectrum peaks at small scales, and the α-model correctly captures the overall shape of the spectrum as well as the scale where the magnetic energy peaks. In the kinematic regime, all the magnetic k-shells in Fourier space (up to $k \lesssim 12$) grow with the same rate, and this feature is also well captured by the α-model simulations (not shown). This evolution is characteristic of small scale dynamos, as well as a $k^{3/2}$ slope in the magnetic energy spectrum at early times [36, 37]. Fig. 18.b shows the late-time spectra, when approximate equipartition has been achieved. Note that as a result of helical dynamo action, a magnetic field at large scales ($k = 1$) is generated (see Fig. 18.b). The amplitude of this mode is in good agreement for both DNS and α-model simulations.

Figure 19 shows surfaces of constant magnetic energy at $t = 60$, when the nonlinear saturation has already taken place

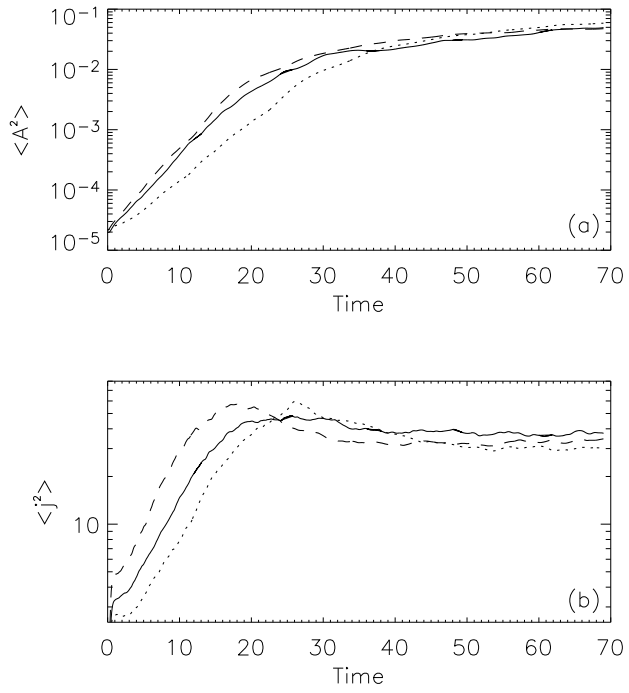

FIG. 17: (a) Mean square vector potential, and (b) mean square current density as functions of time. Labels are as in Fig. 13.

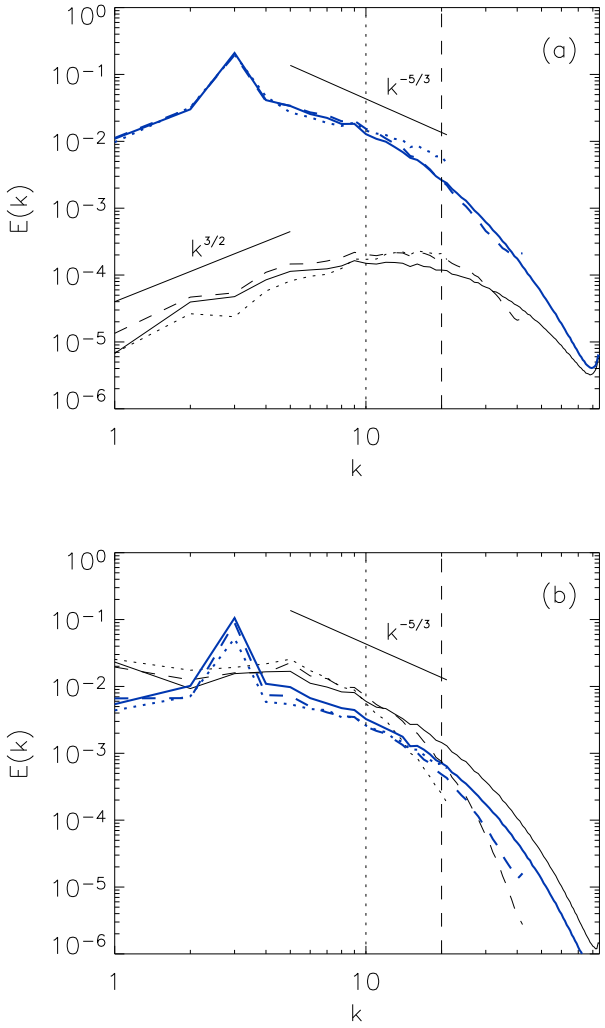

FIG. 18: (color online) Kinetic (thick blue lines), and magnetic energy spectra (thin lines), at (a) $t = 6$ and (b) $t = 70$. Kolmogorov's $k^{-5/3}$ and Kazantsev's $k^{3/2}$ spectra are shown as a reference. The vertical dotted and dashed lines correspond to the scales $\alpha^{-1} = 10$ and 20 respectively. Labels are as in Fig. 13.

but the large scale magnetic field is still growing. Thin and elongated structures can be identified in the magnetic field growing in the DNS. However, note that while these structures are present both in the DNS and in the alpha-model, in the latter case the structures are thicker. This change is related to the filtering length α in the alpha-model. Similar results have been found in vorticity structures observed in simulations of hydrodynamic turbulence using the alpha-model [6].

We thus conclude that there are few surprises in the dynamo simulations, at least for these values of η/ν, and no glaring departures of the α-model predictions from the DNS results.

VII. SUMMARY; DISCUSSION

Within the framework of rectangular periodic boundary conditions, we have examined four familiar three-dimensional MHD turbulence effects via the α-model and DNS. In every case, the principal large-scale features of these phenomena have been achieved with the α-model to acceptable accuracy. The savings in computer time achieved by the α-model runs have ranged from $256^3/128^3 = 8$ to $256^3/64^3 = 64$, without considering extra saving in the time step from the CFL condition as the resolution is decreased. In no case has the α-model yielded results at significant variance with the DNS runs, which have been regarded as accurate.

Other features of the DNS runs, such as the probability distribution functions of the fluctuating quantities (such as local energy dissipation rates), have also been reproduced by the α-model as they were in two dimensions [14], but we have not shown those results here because they are so similar to what was found in two dimensions.

In Ref. [14] also the errors of the α-model computations were compared against under-resolved DNS. The behavior of the α-model in three dimensions is comparable to our previous results, and therefore we refer the reader to our previous work for a detailed discussion about this topic.

In conclusion, the MHD α-model can be considered to be validated, at least for the behavior of long-wavelength spectra in periodic boundary conditions. Its implementation in the presence of material boundaries stands as a next forbidding challenge.

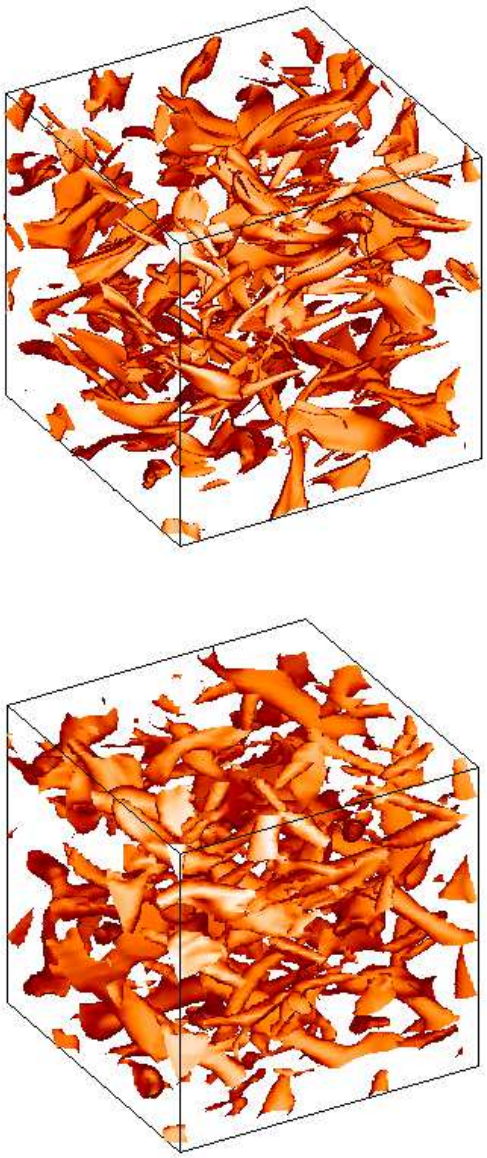

FIG. 19: (color online) Surfaces of constant magnetic energy at $t = 60$ at 50% of its maximum value, for the DNS (above), and the 64^3 alpha-model (below).

Acknowledgments

We thank H. Tufo for providing computer time at UC-Boulder, NSF ARI grant CDA-9601817. Computer time was also provided by NCAR and Dartmouth. The NSF grants ATM-0327533 at Dartmouth College and CMG-0327888 at NCAR supported this work in part and are gratefully acknowledged.

[1] D.D. Holm, J.E. Marsden and T.S. Ratiu, "The Euler-Poincaré Equations and Semidirect Products with Applications to Continuum Theories," *Adv. in Math.* **137**, 1-81 (1998).

[2] D.D. Holm, J.E. Marsden and T.S. Ratiu, "Euler-Poincaré Models of Ideal Fluids with Nonlinear Dispersion," *Phys. Rev. Lett.* **80**, 4173-4176 (1998).

[3] S.Y. Chen, D.D. Holm, C. Foias, E.J. Olson, E.S. Titi, and S. Wynne, "The Camassa-Holm equations as a closure model for turbulent channel and pipe flows," *Phys. Rev. Lett.* **81**, 5338-5341 (1998).

[4] S.Y. Chen, C. Foias, D.D. Holm, E. Olson, E.S. Titi, S. Wynne, "The Camassa-Holm equations and turbulence," *Physica D* **133** 49-65 (1999).

[5] S.Y. Chen, C. Foias, D.D. Holm, E.J. Olson, E.S. Titi, and S. Wynne, "A connection between the Camassa-Holm equations and turbulence in pipes and channels," *Phys. Fluids* **11**, 2343-2353 (1999).

[6] S.Y. Chen, D.D. Holm, L.G. Margolin, and R. Zhang, "Direct numerical simulations of the Navier-Stokes alpha model," *Physica D* **133**, 66-83 (1999).

[7] C. Foias, D.D. Holm, and E.S. Titi, "The Navier-Stokes-alpha model of fluid turbulence," *Physica D* **152**, 505-519 (2001).

[8] B. T. Nadiga and S. Shkoller, "Enhancement of the inverse cascade of energy in the two-dimensional Lagrangian-averaged

Navier-Stokes equations," *Phys. Fluids* **13**, 1528-1531 (2001).

[9] D.D. Holm, "Averaged Lagrangians and the mean dynamical effects of fluctuations in ideal fluid dynamics," *Physica D* **170**, 253-286 (2002).

[10] D. D. Holm, "Lagrangian averages, averaged Lagrangians, and the mean effects of fluctuations in fluid dynamics," *Chaos* **12**, 518-530 (2002).

[11] C. Foias, D.D. Holm, and E.S. Titi, "The three-dimensional viscous Camassa-Holm equations and their relation to the Navier-Stokes equations and turbulence theory," *J. Dynamics and Diff. Equ.* **14**, 1-35 (2002).

[12] A.A. Ilyin and E.S. Titi, "Attractors to the two-dimensional Navier-Stokes-α model: An α-dependence study," *J. Dynamics Diff. Equ.* **15**, 751-777 (2003).

[13] K. Mohseni, B. Kosović, S. Shkoller, and J.E. Marsden, "Numerical simulations of the Lagrangian averaged Navier-Stokes equations for homogeneous isotropic turbulence," *Phys. Fluids* **15**, 524-544 (2003).

[14] P.D. Mininni, D.C. Montgomery, and A.G. Pouquet, "A numerical study of the alpha model for two-dimensional magnetohydrodynamic turbulent flows," *Phys. Fluids*, submitted (arXiv:physics/0410159).

[15] Y. Ponty, P.D. Mininni, D.C. Montgomery, J.-F. Pinton, H. Politano, and A. Pouquet, "Numerical study of dynamo action at low magnetic Prandtl numbers," *Phys. Rev. Lett.*, submitted (arXiv:physics/0410046).

[16] D. Montgomery and A. Pouquet, "An alternative interpretation for the Holm 'alpha model'," *Phys. Fluids* **14**, 3365–3366 (2002).

[17] W.H. Matthaeus and D. Montgomery, "Selective decay hypothesis at high mechanical and magnetic Reynolds numbers," *Ann. N.Y. Acad. Sci.* **357**, 203 (1980).

[18] A.C. Ting, W.H. Matthaeus, and D. Montgomery, "Turbulent relaxation processes in magnetohydrodynamics," *Phys. Fluids* **29**, 3261 (1986).

[19] R. Kinney, J.C. McWilliams and T. Tajima, "Coherent structures and turbulent cascades in two-dimensional incompressible magnetohydrodynamic turbulence," *Phys. Fluids* **2**, 3623-3639 (1995).

[20] R. Grappin, A. Pouquet, and J. Léorat, " Dependence on Correlation of MHD Turbulence Spectra," *Astron. Astrophys.* **126**, 51-56 (1983).

[21] A. Pouquet, M. Meneguzzi, and U. Frisch, " The Growth of Correlations in MHD Turbulence," *Phys. Rev. A* **33**, 4266-4276 (1986).

[22] S. Ghosh, W.H. Matthaeus, and D.C. Montgomery, "The evolution of cross helicity in driven/dissipative two-dimensional magnetohydrodynamics," *Phys. Fluids* **31**, 2171-2184 (1988).

[23] D.K. Lilly, "Numerical simulation of two-dimensional turbulence," *Phys. Fluids Suppl. II* **12**, 240-249 (1969).

[24] U. Frisch, A. Pouquet, J. Léorat, and A. Mazure, "On the possibility of an inverse cascade in MHD helical turbulence," *J. Fluid Mech.* **68**, 769–778 (1975).

[25] A. Pouquet, U. Frisch, and J. Léorat, "Strong MHD helical turbulence and the nonlinear dynamo effect," *J. Fluid. Mech.* **77**, 321-354 (1976).

[26] M. Hossain, W.H. Matthaeus, and D. Montgomery, "Long-time states of cascades in the presence of a maximum length scale," *J.Plasma Phys.* **30**, 479-493 (1983).

[27] A. Brandenburg and K. Subramanian, "Astrophysical magnetic fields and nonlinear dynamo theory," astro-ph/0405052.

[28] M. Meneguzzi, U. Frisch, and A. Pouquet, "Helical and nonhelical turbulent dynamos," *Phys. Rev. Lett.* **47**, 1060–1064 (1981).

[29] B. Galanti, P.L. Sulem, and A. Pouquet, "Linear and nonlinear dynamos associated with ABC flows," *Geophys. Astrophys. Fluid Dyn.* **66**, 183-208 (1992).

[30] O. Podvigina and A. Pouquet, "On the non-linear stability of the 1:1:1 ABC flow," *Physica D* **75**, 471-508 (1994).

[31] V. Archontis, S.B.F. Dorch, and Å. Nordlund, "Dynamo action in turbulent flows," *Astron. Astrophys.* **410**, 759-766 (2003).

[32] A. Brissaud, U. Frisch, J. Léorat, M. Lesieur, and A. Mazure, "Helicity cascades in fully developed isotropic turbulence," *Phys. Fluids* **16**, 1366-1367 (1973).

[33] J.C. André and M. Lesieur, "Influence of helicity on the evolution of isotropic turbulence at high Reynolds number," *J. Fluid Mech.* **81**, 187-207 (1977).

[34] Q. Chen, S. Chen, G.L. Eyink, "The joint cascade of energy and helicity in three-dimensional turbulence," *Phys. Fluids* **15**, 361-374 (2003).

[35] D.O. Gómez and P.D. Mininni, "Understanding turbulence through numerical simulations," *Physica A* **342**, 69-75 (2004).

[36] A. Brandenburg, "The inverse cascade and nonlinear alpha-effect in simulations of isotropic helical hydromagnetic turbulence," *Astrophys. J.* **550**, 824-840 (2001).

[37] A.P. Kazanstev, "Enhancement of a magnetic field by a conducting fluid," *Sov. Phys. JETP* **26**, 1031-1034 (1968).